In Vivo Label-free Functional Photoacoustic Monitoring of Ischemic Reperfusion

13 authors, including:

Renzhe Bi
Singapore Bioimaging Consortium
34 PUBLICATIONS   **222** CITATIONS

SEE PROFILE

Dinish U. S
Agency for Science, Technology and Research (A*STAR)
109 PUBLICATIONS   **1,526** CITATIONS

SEE PROFILE

Chi Ching Goh
National University of Singapore
44 PUBLICATIONS   **701** CITATIONS

SEE PROFILE

Mohesh Moothanchery
Agency for Science, Technology and Research (A*STAR)
30 PUBLICATIONS   **173** CITATIONS

SEE PROFILE

Some of the authors of this publication are also working on these related projects:

Noncontact Photoacoustic Microscope View project

Optical Biopsy View project

In Vivo Label-free Functional Photoacoustic Monitoring of Ischemic Reperfusion

Renzhe Bi[1†], U. S Dinish[1†], Chi Ching Goh[2†], Toru Imai[3], Mohesh Moothanchery[1], Xiuting Li[1], Jin Young Kim[4], Seungwan Jeon[4], Yang Pu[5], Chulhong Kim[4], Lai Guan Ng[2], Lihong V. Wang[3*], Malini Olivo[1*]*

[1] Singapore Bioimaging Consortium, 11 Biopolis Way, 138667, Singapore
[2] Singapore Immunology Network, 8a Biomedical Grove, 138648, Singapore
[3] Caltech Optical Imaging Laboratory, Andrew and Peggy Cherng Department of Medical Engineering and Department of Electrical Engineering, California Institute of Technology, 1200 East California Boulevard, Pasadena, CA 91125, USA
[4] Department of Creative IT Engineering, Pohang University of Science and Technology, 77 Cheongam-ro, Nam-gu, Pohang, Gyeongbuk, 37673, Republic of Korea
[5] MicroPhotoAcoustics Inc., 105 Comac Street, Ronkonkoma, NY 11779, USA
[†] Equally contributing authors
[*] Correspondence: Malini Olivo: malini_olivo@sbic.a-star.edu.sg; Lihong V. Wang: LVW@caltech.edu; Lai Guan Ng: Ng_Lai_Guan@immunol.a-star.edu.sg

Key words: photoacoustic imaging, ischemia reperfusion, skin, image processing

Pressure ulcer (PU) formation is a common problem among patients confined to bed or restricted to wheelchairs. The ulcer forms when the affected skin and underlying tissues go through repeated cycles of ischemia and reperfusion, leading to inflammation. This theory is evident by intravital imaging studies performed in immune cell-specific, fluorescent reporter mouse skin with induced ischemia-reperfusion (I-R) injuries. However, traditional confocal or multi-photon microscopy cannot accurately monitor the progression of vascular reperfusion by contrast agents, which leaks into the interstitium under inflammatory conditions. Here, we develop a dual-wavelength micro electro mechanical system (MEMS) scanning based optical resolution photoacoustic microscopy (OR-PAM) system for continuous label-free functional imaging of vascular reperfusion in an IR mouse model. This MEMS-OR-PAM system provides fast scanning speed for concurrent dual-wavelength imaging, which enables continuous monitoring of the reperfusion process. During reperfusion, the revascularization of blood vessels and the oxygen saturation (sO_2) changes in both arteries and
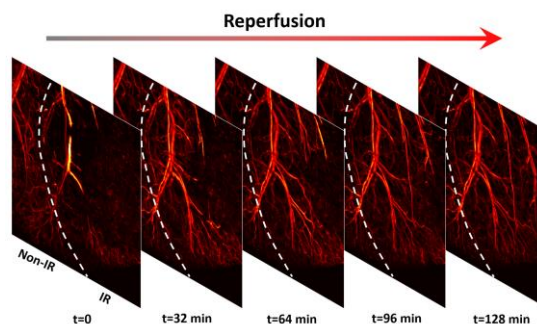

Illustration of the vascular reperfusion of the ear skin.

veins are recorded, from which the local oxygen extraction ratios of the ischemic tissue and the unaffected tissue can be quantified. Our MEMS-OR-PAM system provides novel perspectives to understand the I-R injuries. It solves the problem of dynamic label-free functional monitoring of the vascular reperfusion at high spatial resolution.

1. Introduction

Ischemia-reperfusion (I-R) injuries occur in a range of pathophysiological (e.g. myocardial infarctions, strokes and pressure ulcers) and surgically induced (e.g. organ transplantations) conditions [1,2]. It involves a transient blockade of blood vessels leading to a drop of oxygen delivery to the tissues and a subsequent re-flow of blood. Prolonged ischemia induces cell death, while the ensuing reperfusion induces reactive oxygen species (ROS)

production, and as a consequence, induces inflammation [3,4]. Current intravital imaging technique such as multiphoton microscopy (MPM) allows direct visualization of recruitment of innate immune cells during the early phases of reperfusion. However, this approach does not provide information about the reperfusion/re-oxygenation process, making it impossible to understand the dynamics of blood vessel reperfusion and immune cell infiltration. MPM is one of the most popular optical imaging modalities for monitoring tissue vasculature *in vivo*. For the visualization of the vasculature by MPM, various types of contrast agents, such as Evans Blue, have to be injected into the experimental animals. The limitation of this approach is the loss of contrast between blood vessels and interstitium under inflammatory conditions due to the leakage of the labeling agents into the interstitium in response to increase vascular permeability [5,6]. This challenge is best illustrated in Supplementary Fig S1.

Oxygen plays a central role in I-R injury [7,8]. Against common expectations, oxygenated blood tends to cause more damage to the tissue than deoxygenated blood during the process of reperfusion due to the ROS [3,9]. Meanwhile, the oxygen saturation (sO_2) is an indicator of the tissue viability [8]. Conceivably, sO_2 imaging will provide unprecedented views into the process of ischemic reperfusion. However, contrast agents like Evans Blue cannot distinguish oxy-hemoglobin and deoxy-hemoglobin states and hence, functional measurement of oxygen levels within the vasculatures could not be achieved. For high resolution imaging of vascular sO_2 in I-R tissue, only frozen micro-spectrophotometry has been reported [10]. However, it is an *in vitro* method, thus continuous monitoring of reperfusion can't be conducted.

To date, there is an unmet need for an imaging technique, which is capable of detecting the I-R and associated sO_2 changes in a label-free manner at high speed. Therefore, we developed a dual-wavelength microelectromechanical system (MEMS) scanning optical-resolution photoacoustic microscopy (OR-PAM) imaging system to monitor the vascular I-R in the tissue and image the sO_2 changes in the blood vessels in a mouse model. OR-PAM is a hybrid imaging modality that combines optical and ultrasound imaging [11–18]. It has been reported for various biomedical label-free imaging applications [19–25]. A focused nanosecond pulsed laser beam illuminates the sample in OR-PAM. The laser pulse stimulates the absorber within the illumination spot. The stimulated acoustic wave then propagates through the coupling medium into an ultrasound transducer. By two dimensional scanning of

the region, a 3D image can be formed, whose lateral resolution is determined by the size of the optical spot [26–30].

Traditional OR-PAM system scans the object by mechanical motors [31–33], which is slow for continuous imaging. When a multi-wavelength laser source is used for functional OR-PAM, limited by wavelength tuning speed, pulse-by-pulse wavelength switching can't be achieved. In this case, the total imaging time will increase two times for dual-wavelength imaging [31,34]. In this paper, we combine two single-wavelength pulsed lasers (532 nm and 559 nm) into one beam and switch the excitation wavelength at each A-line scan. By this, the total imaging time is the same as single wavelength scanning. The fast dual-wavelength imaging capability enables continuous monitoring of the reperfusion process. A frangi filter (multi-scale ridge enhancement algorithm) [35] is implemented for vascular segmentation.

The primary goal of this study is to investigate the reperfusion process in the context of sO_2 and vasculature *in vivo* by employing our customized dual-wavelength functional MEMS-OR-PAM imaging system. To achieve this goal, we adapted a well-established mouse ear skin-I-R model, which has previously been used for monitoring immune cell infiltration post reperfusion [1,36]. With this model, we observed the vascular and sO_2 changes in blood vessels during reperfusion. A video of how the ischemic blood vessels recovered step by step is presented. A higher local oxygen extraction ratio in the ischemic tissue comparing with the nearby unaffected tissue is reported.

We believe that in the future this technique could be developed as hand held and fast imaging scanners that have a tremendous potential in understanding the I-R, especially to predict the occurrence of pressure ulcer (PU) and treatment prognosis in clinical settings.

2. Imaging system

The dual-wavelength MEMS-OR-PAM system was retrofitted based on a commercial mechanical-scanning PAM system (MicroPhotoAcoustics, Inc., USA) [37]. A customized water-immersible MEMS scanner (OPTICHO, Republic of Korea) [38,39] was installed to achieve high imaging speed for dual-wavelength imaging. To quantify sO2 in the blood vessels, the pulse-to-pulse energy variation of the nanosecond laser source needed to be compensated for. Therefore, a photodiode was mounted on top of the PA sensor to record the energy of every laser pulse during scanning. To maintain a stable environment for the mouse ear skin imaging, a

customized ear holder which maintains a constant temperature was designed and implemented. The schematic of the imaging system is demonstrated in Fig 1.
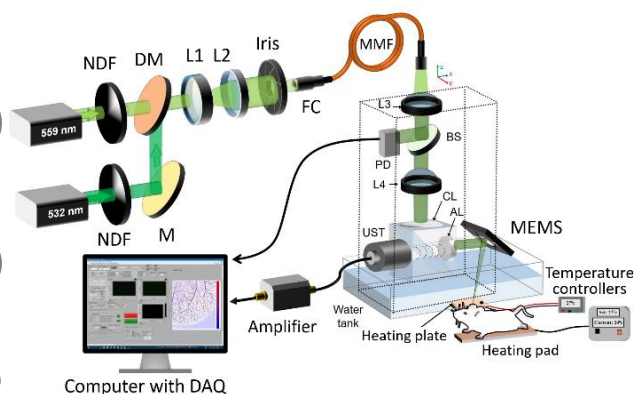
Figure 1. Schematic of the dual-wavelength MEMS-OR-PAM imaging system. NDF: neutral-density filter, M: mirror, DM: dichroic mirror, L1 – L4: lens, FC: fiber collimator, MMF: multi-mode fiber, PD: photodiode, BS: beam splitter, CL: correction lens, AL: acoustic lens, UST: ultrasound transducer.

The system used two Q-switched DPSS lasers at 532 nm and 559 nm (Advanced Optowave, USA) combined by a dichroic mirror (86-327, Edmund Optics) into a single beam. Both lasers operate at 10 kHz and 50 nJ per pulse. The optical lateral resolution is 5.2 μm. During imaging, the optical focus is usually ~ 200 μm underneath the surface of the skin. Therefore, the calculated laser fluence is about 12 mJ/cm^2, which is lower than the ANSI safety limit (20 mJ/cm^2).

The use of multiple lasers instead of a single tunable laser enabled fast switching between excitation wavelengths for accurate sO$_2$ measurements. Therefore, PA signals generated from both lasers would be received at each A-line scanning successively, which guarantees alignment between the PA images acquired at different wavelengths. The combined beam was expanded and collimated using a double concave lens, L1 (LD2297, Thorlabs) and a plano-convex lens, L2 (LA1509, Thorlabs). The collimated beam was coupled to an optical fiber with a core diameter of 10 μm using a fiber coupler (F240FC-532, Thorlabs). The delivery path of the laser into the PA sensor is indicated by the dashed cuboid in Fig 1. Along the optical path in the PA sensor, a beam splitter with 95% transmission and 5% reflection rates is used to guide a small portion of light into the photodiode (APD120A/M, Thorlabs) for pulse energy calibration. An optical-acoustic combiner, which reflects light but transmits acoustic wave, consisted of an aluminum-coated right-angle prism (NT32-331, Edmund Optics) and an uncoated right-angle prism (NT32- 330, Edmund Optics). A plano-convex lens (NT67-147, Edmund Optics) was attached to the top of the combiner

for aberration corrections. An acoustic lens (NT45-010, Edmund Optics) was attached to the right side of the combiner and an ultrasonic transducer (V214-BC-RM, Olympus-NDT) was attached to the left side of the combiner. The MEMS scanning mirror was coated with aluminum with a reflection rate of 92% and 84% for laser and ultrasound, respectively. To achieve better coupling of the ultrasound signal generated from biological tissue, a water bath was prepared. A transparent film was applied to separate the water from the imaging area. The optical-acoustic beam combiner was immersed in the water bath. A computer with LabVIEW controls the MEMS scanner, motor stage, trigger for laser pulsing and acquisition of acoustic as well as photodiode signals.

A single-axis MEMS scanner was utilized to achieve fast optical scanning. A motor controlled the movement at the orthogonal direction as the MEMS scanner. The combination of MEMS (fast axis) and mechanical (slow axis) scanning guaranteed high imaging speed and minimized imaging distortion. Due to the limited scanning distance of the MEMS scanner (~ 2 mm), multiple stacks needed to be acquired and stitched together to produce an image with an extended field of view.

3. Animal preparation and imaging protocol

Animal imaging procedures were performed according to the guidelines of approved Institutional Animal Care and Use Committee protocol #151085.

8-12-week old B6(Cg)-Tyr^{c-2J}/J (The Jackson Laboratory) albino mice were anaesthetized with an intra-peritoneal injection of ketamine-xylazine (15 mg mL^{-1} ketamine and 1 mg mL^{-1} xylazine; 8 μL g^{-1} bodyweight). Ears were depilated using hair removal cream (Veet, USA) prior to I-R to improve PA signal collection. The I-R process was performed as previously described [1,36]. Briefly, magnets with a Gauss rating of approximately 3000 were used to simulate the I-R process. Ischemia was induced by clamping the ear between 2 magnets for 1.5h. The clamping location is illustrated in Fig 2.
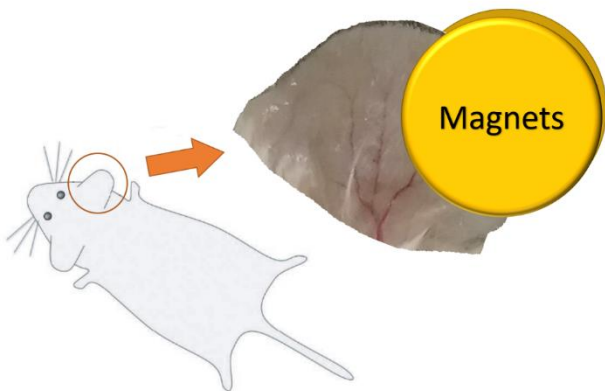
Figure 2. Illustration of the ear-clamping location for animal preparation. Two pieces of magnets clamp part of the ear for 1.5h to induce ischemia in the skin.

Magnets were then removed to allow reperfusion to take place. Immediately after the magnets were removed, the mouse was transferred to a custom-built imaging platform which was fitted with heating systems to maintain both core and ear temperature at 37°C and 35°C respectively. The ear was positioned on the imaging platform with a layer of ultrasound gel on top. A water-filled well with a transparent bottom was filled with deionized water and placed over the mouse ear. The PA sensor head, including the MEMS scanner, the optical-acoustic combiner including ultrasound transducer, was immersed into the water bath during imaging. Images were captured at intervals of 4 minutes during the 2-hour reperfusion process. The imaging region (5 × 4 mm) covered the ischemic region, the boundary of the ischemic region and the unaffected region. The same imaging protocol was repeated independently in 5 different mice. To validate the temporal sO_2 behavior during reperfusion, the measurement of a control group of mice was also performed. Unlike the I-R group, the control group was directly imaged by dual-wavelength MEMS-OR-PAM without magnetic clamping of its ear. The other experimental conditions were unchanged in the control imaging group as well.

4. Image processing

The raw OR-PAM data was a 3D matrix of the ultrasound signal amplitude. To remove the noise of each one-dimensional scan (B-scan) images, each slice was filtered by a band-pass finite impulse response (FIR) filter. Then a maximum amplitude projection (MAP) was performed along the z axis to generate a 2D x-y image. To cancel the pulse-to-pulse variation of the laser energy, the 2D photodiode amplitude record was used to

normalize the MAP image, which gives an amplitude normalized vascular image. With the normalized vascular image at 532 nm, a customized Frangi filter [35] was applied to enhance the contrast of the ridge structures (blood vessels) and suppress the non-vascular structures that are outside the predefined scale range. Then a global threshold is applied to the Frangi-filtered image to extract the vascular mask, which is used for blood vessel segmentation from the normalized MAP image.

Based on the optical absorption of oxy-hemoglobin and deoxy-hemoglobin at 532 nm and 559 nm [40], the relative concentration of each component can be derived from the dual-wavelength images by using a spectral unmixing algorithm pixel by pixel [31,41]. The sO_2 is defined as:

$$sO_2 = \frac{C_{oxy-hemoglobin}}{C_{oxy-hemoglobin} + C_{deoxy-hemoglobin}}, \quad (1)$$

where $C_{oxy-hemoglobin}$ is the concentration of oxy-hemoglobin and $C_{deoxy-hemoglobin}$ is the concentration of deoxy-hemoglobin. The image process is illustrated in Fig 3.

From the vascular sO_2 image, the local oxygen extraction ratio can be quantified. It is defined as [42,43]:

$$ERO_2 = \frac{sO_{2,a} - sO_{2,v}}{sO_{2,a}}, \quad (2)$$

where ERO_2 represents extraction ratio of oxygen, $sO_{2,a}$ and $sO_{2,v}$ are the oxygen saturation of a pair of artery and vein, respectively. ERO_2 is a measure of the fraction of oxygen delivered to the microcirculation that is taken up by the tissues [42,43].
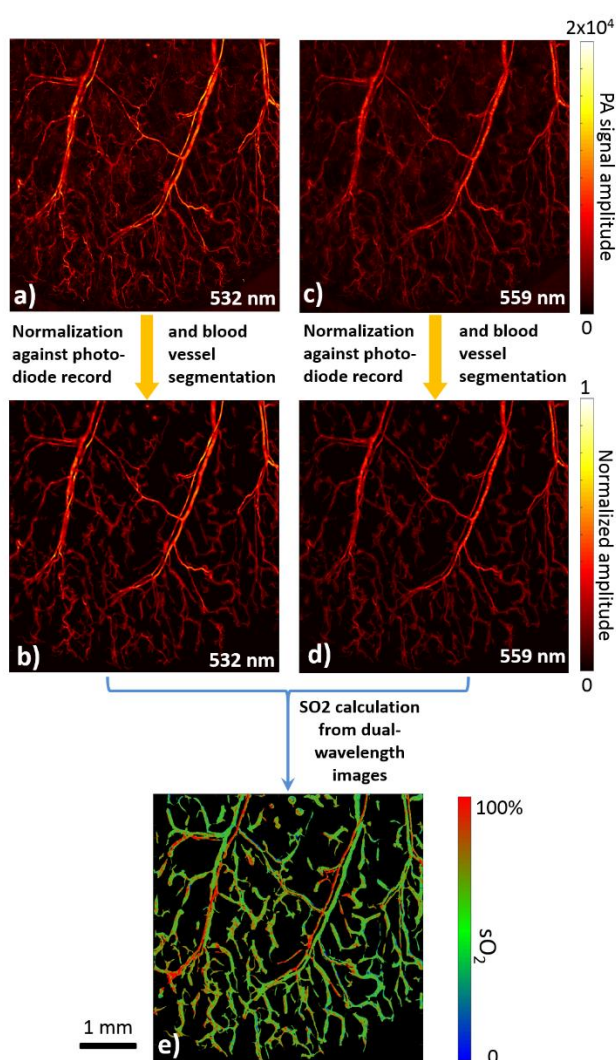
Figure 3. Illustration of the sO$_2$ image processing. a) and c) are the MAP images of 532 nm and 559 nm, respectively. b) and d) are the amplitude-normalized and vessel-segmented images of 532 nm and 559 nm, respectively. e) is the sO2 image generated from b) and d). The color scale bar under e) indicates the sO$_2$ value from 0 to 100%.

5. Result

With the dual-wavelength MEMS-OR-PAM system, we could observe in real time vascular reperfusion with high spatial resolution. The gradual recovery of the vasculature and the re-oxygenation of blood vessels at each corresponding time point are demonstrated in Fig 4 a-c and d-f, respectively. The time-lapse videos are provided in Supplementary Information (Video 1 and Video 2).

Immediately post I-R, no blood vessels were visible within the magnet-clamped region, indicating that there was no oxygen delivery to the ischemic tissues (Fig 4a, t=0). The boundary between the ischemic and unaffected region was clearly delineated by a truncation of the blood vessels at the boundary separating the two regions (Fig 4a).

From our in-depth analysis, we observed that reperfusion commenced in blood vessels of the largest diameter, regardless of whether it was an artery or vein, as distinguished by the difference in their sO2 levels (Fig 4 d-f). Conversely, reperfusion was slowest in the capillaries, the average diameter of which was smaller.
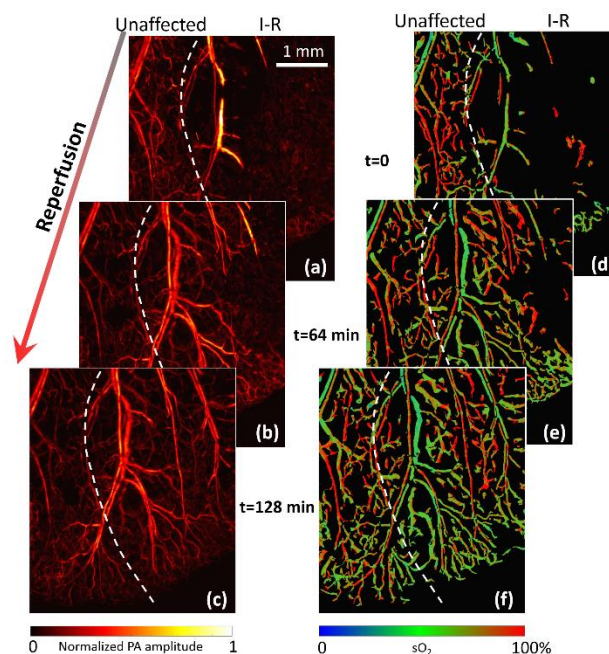

Figure 4. (a) – (c) The vascular recovery and (d) – (f) the sO$_2$ map at the corresponding time points are shown at t = 0, 64, 128 min. A dashed line is drawn in each image to indicate the I-R region and the non-I-R unaffected region. The full video of the vascular and sO$_2$ change during the reperfusion can be found in supplementary videos 1 and 2.

Next, we compared the oxygen saturation level of arteries/veins located in the I-R region and the nearby unaffected region (Fig 5). Measurements were taken at the start of reperfusion of each of these blood vessels. Because of the blood vessel segmentation processing, sO$_2$ value is averaged only within the pixels inside the vascular. Post reperfusion, sO$_2$ level in the arteries were similar in the 2 different zones, with an average of ~90%, suggesting a full and rapid recovery of oxygen delivery to the ischemic region (Fig 5 c-d). However, interestingly, within the ischemic zone (Fig 5 d), we detected a drop in the sO$_2$ level of re-perfused veins over time. Unlike arteries where the oxygen saturation was maintained at normal levels, the sO$_2$ level of the veins inside the ischemic region did not return to 70% within the first 2 hours of reperfusion. It stays stably at a lower rate comparing with the veins in unaffected region.

When the oxygen delivery is stable, as shown in the artery plots in Fig 5 c-d, a decreasing sO_2 trend in veins indicates higher ERO_2 from the tissue (Fig 5 e-f). The average ERO_2 is 26.10 ± 5.01% in the unaffected tissue and 37.21 ± 10.62% in the I-R tissue. The p-value of these two sets of measurements is 4.99×10^{-20}, indicating ERO_2 in I-R tissue is significantly higher than that in unaffected tissue.

Our observation is in line with a previous study in cerebral ischemia and reperfusion, which reported a higher oxygen extraction rate from the ischemic side of the cortex comparing with the contralateral cortex during reperfusion [10]. However, the previous cerebral study used frozen micro-spectrophotometry method to image the *ex vivo* brain slides. MEMS-OR-PAM provides a non-invasive option for continuous *in vivo* imaging of vascular sO_2.

Note the plots in Fig 5 c-f are averaged over 5 independent observations on different animals. The blood vessel selection of other animals is further illustrated in Supplementary Fig S2.

To validate the temporal sO_2 behavior during reperfusion, the measurement of a control group was performed. Unlike the I-R group which went through the ischemia-inducing process by magnet-clamping, the control group was directly imaged by dual wavelength MEMS-OR-PAM system without any treatment. The same temperature condition was maintained as the I-R group. The ear skin was imaged continuously for 2 hours.

A representative vascular image and sO_2 image of the control mouse are shown in Fig 6 (a) and (b), respectively. A pair of artery and vein is selected from the image to generate the temporal sO_2 plot (Fig 6c). Both the artery and vein have relatively stable sO_2 readings along the time, which confirms the performance of the MEMS-OR-PAM system. The ERO_2 calculated from the selected vessels is shown in Fig 6(d), with an average value of 28.8 ± 5.08%.
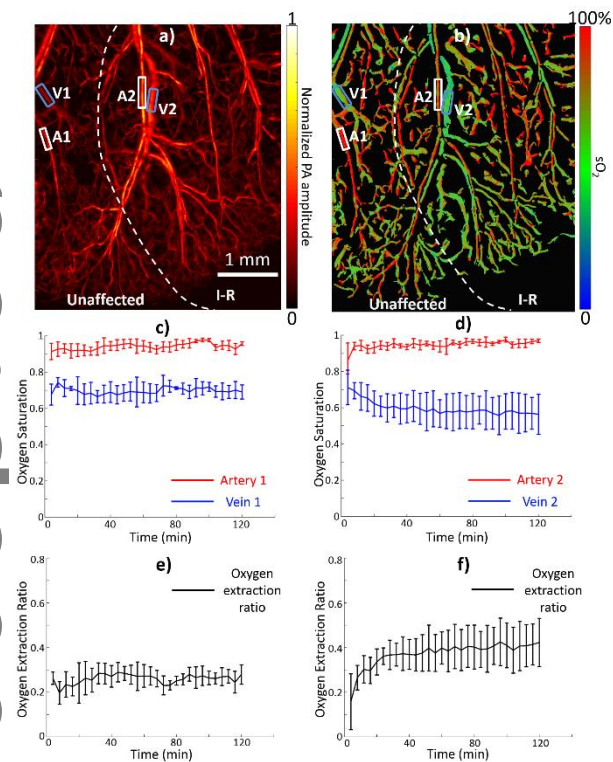

Figure 5. (a) Single wavelength vascular image at the end of reperfusion and (b) sO_2 vascular image at the end of reperfusion. The selected areas of the blood vessel for sO_2 plotting are indicated by square boxes in (a) and (b). The temporal sO_2 readings in A1 and V1 (unaffected region) are plotted in (c). The temporal sO_2 readings in A2 and V2 (connected to I-R region) are plotted in (d). The oxygenation level of the residual artery blood is lower than 90% before the reperfusion. However, the sO_2 of arteries recovers immediately after the reperfusion starts. The local oxygen extraction ratios of the unaffected tissue and I-R tissue are plotted in (e) and (f), respectively. The plots in (c) – (f) are averaged over 5 independent observations on different animals.
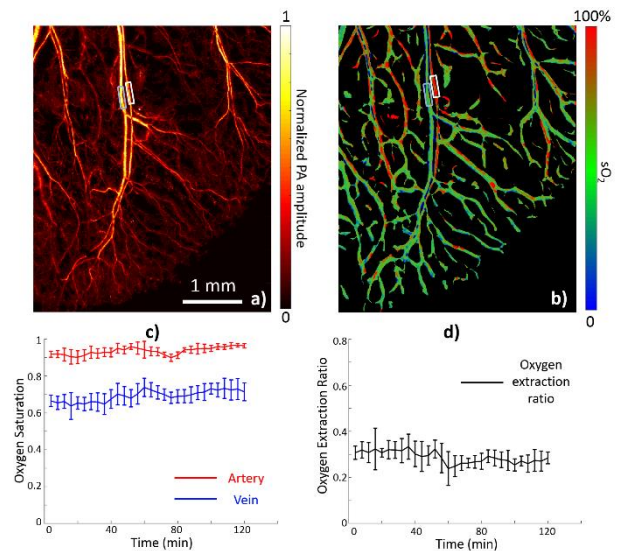

Figure 6. (a) PA vascular image and (b) sO_2 image of a representative control mouse ear skin without any ischemia-inducing process. (c) Temporal sO_2 plot of the selected artery and vein for 2 hours. (d) Temporal plot of local oxygen extraction ratios calculated from the selected arteries and veins.

Our study focused on the vascular and sO_2 changes during the reperfusion period of I-R. Limited by the standard laser repetition rate of 10 kHz, the interval between two image frames in our setting is 4 min. However, the reperfusion usually lasts around 2 hours

under a constant temperature of ~35 degree Celsius. Typical conventional MPM imaging study uses a frame interval of 5 min. Therefore, the current imaging speed employed in dual-wavelength MEMS-OR-PAM meets the requirement of the experiment. Further, in our ongoing studies, lasers with higher repetition rate will improve the imaging frame rate.

6. Discussion

The repeated cycles of I-R are the main factor that leads to pressure ulcer (PU). PU causes significant problems to the healthcare sector, specifically in an aging population as it affects the quality of life in persons who are bedridden or restricted to wheelchairs [44–46]. Though there are several possible reasons for the occurrence of PU, it is accounted to the compression of underlying soft tissue with bony structures [47,48], related localized ischemia [45] and subsequent reperfusion injury [4]. Consequently, blood flow that determines the ability of the skin in response to ischemic stress and reperfusion has been proposed to be a predictive tool for identifying people at risk of PU. In this context, the sO_2 information that we derived from this study has great significance in understanding the formation of PU. Normal tissue usually has an ERO_2 of 20% - 30% [42]. However, we discovered that the I-R tissue has a significantly higher ERO_2 (37.21 ± 10.62%) than normal tissue during reperfusion. It suggests our dual-wavelength MEMS-OR-PAM could be potentially developed as a quantitative tool in determining the extension of PU and thereby forming an imaging-derived metrics of sO_2 as a predictive tool.

Wound (diabetic ulcers or venous ulcers) and its healing status could also be linked to the local microvascular perfusion status. It is well understood that a healing wound in general has a higher perfusion status. Our OR-PAM based imaging method could also find application in elucidating the perfusion status of wounds. The gold standard used in clinical settings to monitor diabetic foot ulcers (DFUs) is by visual inspection of changes in the wound site and the physical measurements of the size and its depth. However, clinicians are not able to assess the structural or physiological information of DFU by visual inspection. The assessment for ischemia in such cases can also be assessed by ankle brachial indexes and clinical examination along with Doppler ultrasound and toe pressures measurements [49]. In all these cases, the key marker of healing status-perfusion is not assessed in an objective way.

In the future, functional OR-PAM may predict the PU formation through the vascular oxygenation information at stage I before the deep wound starts. This will enable early stage detection of wound and promote prevention of PU. Comparing with existing fluorescence-ICG-based perfusion imaging methods, photoacoustic imaging modalities have the advantages of contrast-free measurement and sO_2 imaging capability. Therefore, PAI is easier for the patients to accept and suitable for repeated measurements. In this context, we envision that label free imaging up to a depth of 1-3 mm that PAM can provide could play a crucial role in translating it as a clinically viable tool.

7. Conclusion

In this article, we developed a dual-wavelength MEMS-OR-PAM system for high spatial resolution and contrast-free continuous monitoring of revascularization in an I-R mouse ear model. The fast switching between 532 nm and 559 nm lasers for each A-line ensured a perfect alignment of the images over a large area of 5×4 mm at both wavelengths, which provided an sO_2 map without compromising the spatial resolution. A frangi-filtering based blood vessel segmentation method was employed to process the single wavelength vascular images. Local ERO_2 of the I-R region and the nearby unaffected region were calculated from the vascular sO_2 images. During reperfusion of the ischemic tissue, an increasing ERO_2 was observed, which then stabilized around 37% till the end of the observation. The I-R region was discovered to have a significant higher ERO_2 than the unaffected region. This finding may explain why hyperbaric oxygen treatment reduces I-R injuries [7]. Through this study, our dual-wavelength MEMS-OR-PAM imaging system has demonstrated the capability for high resolution dynamic monitoring of the progressive changes in the vascular system. This capability is critical for the study of all vascular and microcirculation related diseases.

We envision that the combination of PAM and two-photon microscopy is necessary for a better understanding of the effect of vascular changes that interacts with the immune cells during reperfusion and how the sO_2 levels affect the movement of neutrophils. Our on-going work in developing such a multi-modal imaging platform will greatly benefit understanding the mechanism behind I-R and it will eventually help to develop better predictive models for the healing status of different wounds.

8. Acknowledgement

References

1. C. C. Goh, J. L. Li, S. Devi, N. Bakocevic, P. See, A. Larbi, W. Weninger, F. Ginhoux, V. Angeli, and L. G. Ng, J. Invest. Dermatol. **135**, 1181 (2015).
2. C. C. Goh, M. Evrard, S. Z. Chong, Y. Tan, L. D. L. Tan, K. W. W. Teng, W. Weninger, D. L. Becker, H. L. Tey, E. W. Newell, B. Liu, and L. G. Ng, Eur. J. Immunol. 1 (2018).
3. H. K. Eltzschig and T. Eckle, Nat. Med. (2011).
4. S. M. Peirce, T. C. Skalak, and G. T. Rodeheaver, Wound Repair Regen. (2000).
5. M. Radu and J. Chernoff, J. Vis. Exp. (2013).
6. D. Ding, C. C. Goh, G. Feng, Z. Zhao, J. Liu, R. Liu, N. Tomczak, J. Geng, B. Z. Tang, and L. G. Ng, Adv. Mater. **25**, 6083 (2013).
7. J. Buras, Int. Anesthesiol. Clin. **38**, 91 (2000).
8. J. Reenalda, P. Van Geffen, M. Nederhand, M. Jannink, M. IJzerman, and H. Rietman, J. Rehabil. Res. Dev. **46**, 577 (2009).
9. J. A. Buras and L. Garcia-Covarrubias, *Ischemia-Reperfusion Injury and Hyperbaric Oxygen Therapy: Basic Mechanisms and Clinical Studies*, First Edit (Elsevier Inc., 2008).
10. H. R. Weiss, J. Grayson, X. Liu, S. Barsoum, H. Shah, and O. Z. Chi, Stroke **44**, 2553 (2013).
11. J. Xia, J. Yao, and L. V Wang, Electromagn Waves (Camb) **147**, 1 (2014).
12. J. Yao and L. V. Wang, Laser Photon. Rev. **7**, 758 (2013).
13. P. Beard, Interface Focus **1**, 602 (2011).
14. H. Estrada, J. Turner, M. Kneipp, and D. Razansky, Laser Phys. Lett. **11**, (2014).
15. M. Moothanchery, R. Bi, J. Y. Kim, S. Jeon, C. Kim, and M. Olivo, Biomed. Opt. Express **9**, 1190 (2018).
16. S. Manohar and D. Razansky, Adv. Opt. Photonics **8**, 586 (2016).
17. J. Rebling, H. Estrada, S. Gottschalk, G. Sela, M. Zwack, G. Wissmeyer, V. Ntziachristos, and D. Razansky, J. Biophotonics e201800057 (2018).
18. M. Pramanik and C. Kim, IEEE Pulse **6**, 38 (2015).
19. J. Laufer, P. Johnson, E. Zhang, B. Treeby, B. Cox, B. Pedley, and P. Beard, J. Biomed. Opt. **17**, 056016 (2012).
20. B. Lan, W. Liu, Y. Wang, J. Shi, Y. Li, S. Xu, H. Sheng, Q. Zhou, J. Zou, and U. Hoffmann, Biomed. Opt. Express **9**, 4689 (2018).
21. T. T. W. W. Wong, R. Zhang, C. Zhang, H.-C. C. Hsu, K. I. Maslov, L. V. L. L. V. Wang, J. Shi, R. Chen, K. K. Shung, Q. Zhou, and L. V. L. L. V. Wang, Nat. Commun. **8**, 1386 (2017).
22. J. Turner, H. Estrada, M. Kneipp, and D. Razansky, Optica **4**, 770 (2017).
23. R. Cao, J. Li, B. Ning, N. Sun, T. Wang, Z. Zuo, and S. Hu, Neuroimage (2017).
24. T. Wang, N. Sun, R. Cao, B. Ning, R. Chen, Q. Zhou, and S. Hu, Neurophotonics (2016).
25. S. Jeon, H. B. Song, J. Kim, B. J. Lee, R. Managuli, J. H. Kim, J. H. Kim, and C. Kim, Sci. Rep. **7**, (2017).
26. L. V Wang and J. Yao, Nat. Methods **13**, 627 (2016).
27. J. Yao, L. Wang, J.-M. Yang, K. I. Maslov, T. T. W. Wong, L. Li, C.-H. Huang, J. Zou, and L. V Wang, Nat. Methods **12**, 407 (2015).
28. D. Soliman, G. J. Tserevelakis, M. Omar, and V. Ntziachristos, Sci. Rep. (2015).
29. M. Omar, J. Rebling, K. Wicker, T. Schmitt-Manderbach, M. Schwarz, J. Gateau, H. López-Schier, T. Mappes, and V. Ntziachristos, Light Sci. Appl. **6**, 1 (2017).
30. R. Ansari, E. Z. Zhang, A. E. Desjardins, and P. C. Beard, Light Sci. Appl. **7**, 75 (2018).
31. S. Hu, K. Maslov, and L. V. Wang, Opt. Lett. **36**, 1134 (2011).
32. W. Liu, D. M. Shcherbakova, N. Kurupassery, Y. Li, Q. Zhou, V. V Verkhusha, and J. Yao, Sci. Rep. **8**, 11123 (2018).
33. T. Chuangsuwanich, M. Moothanchery, A. T. C. Yan, L. Schmetterer, M. J. A. Girard, and M. Pramanik, Appl. Opt. (2018).
34. J. Yao, K. I. Maslov, Y. Zhang, Y. Xia, and L. V. Wang, J. Biomed. Opt. (2011).
35. A. F. Frangi, W. J. Niessen, K. L. Vincken, and M. A. Viergever, in *Int. Conf. Med. Image Comput. Comput. Interv.* (Springer, 1998), pp. 130–137.
36. J. L. Li, C. C. Goh, J. L. Keeble, J. S. Qin, B. Roediger, R. Jain, Y. Wang, W. K. Chew, W. Weninger, and L. G. Ng, Nat. Protoc. **7**, 221 (2012).
37. R. Bi, G. Balasundaram, S. Jeon, H. C. Tay, Y. Pu, X. Li, M. Moothanchery, C. Kim, and M. Olivo, J. Biophotonics **11**, (2018).
38. K. Park, J. Y. Kim, C. Lee, S. Jeon, G. Lim, and C. Kim, Sci. Rep. **7**, 13359 (2017).
39. J. Y. Kim, C. Lee, K. Park, G. Lim, and C. Kim, Sci. Rep. **5**, 7932 (2015).
40. W. G. Zijlstra, A. Buursma, and W. P. Meeuwsen-van der Roest, Clin. Chem. (1991).
41. H. F. Zhang, K. Maslov, M. Sivaramakrishnan, G. Stoica, and L. V. Wang, Appl. Phys. Lett. **90**, (2007).
42. S. A. McLellan and T. S. Walsh, Contin. Educ. Anaesth. Crit. Care Pain **4**, 123 (2004).
43. K. R. Walley and G. Therapy, Am. J. Respir. Crit.

Care Med. **184**, 514 (2011).

44. M. Reddy, S. S. Gill, and P. A. Rochon, JAMA (2006).

45. F. Liao, S. Burns, and Y.-K. Jan, J. Tissue Viability (2013).

46. W. Choi, E.-Y. Park, S. Jeon, and C. Kim, Biomed. Eng. Lett. 1 (2018).

47. F.-F. Cui, Y.-Y. Pan, H.-H. Xie, X.-H. Wang, H.-X. Shi, J. Xiao, H.-Y. Zhang, H.-T. Chang, and L.-P. Jiang, Int. J. Mol. Sci. **17**, 284 (2016).

48. J. Black, M. M. Baharestani, J. Cuddigan, B. Dorner, L. Edsberg, D. Langemo, M. E. Posthauer, C. Ratliff, and G. Taler, Adv. Skin Wound Care (2007).

49. O. A. Mennes, J. J. van Netten, R. H. J. A. Slart, and W. Steenbergen, Curr. Pharm. Des. **24**, 1304 (2018).